Journal of Solid State Chemistry **161,** 341–347 (2001)
doi:10.1006/jssc.2001.9332, available online at http://www.idealibrary.com on IDEAL®

Cellular Paracrystal Formation from Co-Doped CaO Polycrystals

Pouyan Shen[1] and Jun-Yi Wang

Institute of Materials Science and Engineering, National Sun Yat-sen University, Kaohsiung, Taiwan, Republic of China

Received May 1, 2001; in revised form June 29, 2001; accepted August 1, 2001

A paracrystalline array of defect clusters was shown to form in Co-doped CaO polycrystals while prepared by a sintering route at 1300°C in air. Analytical electron microscopic observations indicated the paracrystal predominantly formed at dislocations and in the area left behind the migrating grain boundaries, exhibiting cellular structure. Defect chemistry consideration suggests the paracrystal is due to the assembly of volume- and charge-compensating defects of the 4:1 type with four octahedral vacant sites surrounding one Co^{3+}-filled tetrahedral interstitial site. The interspacing of such defect clusters is approximately 4.3 times the lattice spacing of the average rock salt structure of Co-doped CaO. This spacing between defect clusters is about 2.7 times that of our previously studied Ni-doped CaO.

Key Words: **CaO; Co dopant; volume compensation; cellular structure; paracrystal.**

1. INTRODUCTION

In this work, the $Co_{1-x}O$/CaO composites prepared by sintering and then annealing in air were studied by analytical electron microscopy (AEM). We focused on the effects of Co dopant and grain boundary migration on defect clustering in the rock salt-type lattice of CaO.

Aliovalent dopant cations were known to cause defect clustering and phase changes of ionic crystals at high temperatures. Three-dimensional transition metal monoxides with the rock salt structure have been extensively studied in this regard (1–20). $Fe_{1-x}O$, having a considerable degree of nonstoichiometry ($x \leq 0.15$ (2)), was known to possess defect clusters of the 4:1 type with four octahedral vacant sites surrounding one Fe^{3+}-filled tetrahedral interstitial site (3). When aged at high temperatures, the 4:1 clusters may assemble into larger units (e.g., 13:4, 16:5 and form a paracrystal (4, 5)), which order further into Fe_3O_4 spinel or other ordered phases: p'' and p''' (6, 7). (The paracrystalline distribution is such that the spacing between defect clusters tends to be maintained fairly constant but relative lateral translations may occur more variably; hence there is negligible diffraction intensity beyond first order (4, 5).)

In contrast to $Fe_{1-x}O$, $Ni_{1-x}O$ has a very small x (approx. 0.001 at 1500°C (8)) and the occurrence of defect clustering is uncertain, whether from the theoretical point of view (9, 10) or based on experimental results (11–15). There is, however, clearer experimental evidence of defect clustering in cation-doped $Ni_{1-x}O$. For example, Zr-doped or (Zr,Y) codoped $Ni_{1-x}O$ was found by AEM to transform to a paracrystal and then a Ni_3O_4 spinel when annealed at 1300 or 1600°C (16, 17). In the case of $Co_{1-x}O$ with a moderate x (approx. 0.01 (18)), spontaneous oxidation to form a Co_3O_4 spinel was known to occur by cooling below 900°C (19). The paracrystal and the spinel phase, however, form above 900°C for (Zr,Y)-codoped $Co_{1-x}O$ (20).

Recently we chose the $Ni_{1-x}O$–CaO system, which has a considerable mutual solid solubility (21) for studying the effect of isovalent, but size-mismatched, dopant cations and resultant Ni^{3+} in tetrahedral interstitial sites on defect clustering of the rock salt-type oxide (22). Since the Ca^{2+} ion is much larger in size than the Ni^{2+} ion in coordination number (C.N.) 6 of the oxygen environment (23), there is a compensation of volume misfit of the cations and the resultant formation of cation vacancies and charge-compensating nickel interstitials, which assemble further into paracrystals. Both the Ca-doped $Ni_{1-x}O$ and Ni-doped CaO exhibit paracrystals near the $Ni_{1-x}O$–CaO interface for a beneficial lower activation energy of nucleation at the interface (22).

In the present study, the $Co_{1-x}O$–CaO system, which has a relatively high mutual solid solubility (24) and a larger cation mismatch in C.N. 6, but an eutectic point lower than that of the $Ni_{1-x}O$–CaO system (21), was studied with emphasis on the following points. First, to study whether a Co-doped CaO paracrystal occur and whether it has interspacing of defect clusters different from that of Ni-doped CaO. Second, to show that paracrystal development in Co-doped CaO is affected by a rather high mobility of the grain boundary acting as a predominant nucleation site.

[1] To whom correspondence should be addressed. Fax + 886-7-5254099. E-mail: pshen@mail.nsysu.edu.tw.

0022-4596/01 $35.00

2. EXPERIMENTAL

Reagent grade $Co_{1-x}O$ (Cerac, 99.5%, 325 mesh) and CaO (Cerac, 99.99%, 325 mesh) powders were used to prepare powder mixture batches of $Co_{1-x}O$/CaO (1:9 molar ratio) by mixing and grinding with an agate mortar and pestle. The powder batches were dry pressed at 650 MPa to form pellets approximately 5 mm in diameter and 2 mm in thickness. The defect structures in the Co–Ca–O system might vary with the reaction temperature, surrounding atmosphere, rate of cooling, and sample preparation conditions for microscopic examination. In this regard, we chose to fire the pellets at 1300°C for 5 and 80 h in an open-air furnace and then to cool them in the furnace at a cooling rate of 5°C/min or quenched in air.

X-ray diffraction (XRD, Cu$K\alpha$, 40 kV, 20 mA at 0.05° and 3 s per step in the 2θ angle range 20–145°) was used to identify the phases at room temperature. The calculated lattice parameters from each d-spacing were plotted against $\cos^2\theta/\sin\theta$ and extrapolated to $\theta = 90°$ to obtain the precise lattice parameter a_o (25). Scanning electron microscopy (SEM, JSM6400 at 20 kV) was used to study the distribution of $Co_{1-x}O$ particles in the sintered CaO matrix. Thin sections of the samples were Ar ion-milled to electron transparency. AEM (JEOL 3010 instrument operating at 300 kV) was used for imaging, selected area electron diffraction (SAED), and point-count energy dispersive X-ray (EDX) analysis. The EDX analysis was performed using K shell counts for Co and Ca and the principle of the ratio method without absorption correction (26). The error of composition measurement was estimated to be within $\pm$ 5%.

3. RESULTS

3.1. SEM and XRD

SEM observations indicated all the fired composites contain inter- and intragranular $Co_{1-x}O$ particles in a matrix of CaO grains with considerable mutual solid solubility. XRD indicated that the CaO matrix has a lattice parameter of 0.4792 $\pm$ 0.0001 nm for the sample fired at 1300°C for 5 and 80 h and cooled in the furnace. A fixed lattice parameter, smaller than that of pure CaO (0.4811 nm, JCPDS 37-1497), indicated that the solid solubility limit of Co in CaO had been reached within 5 h at 1300°C. The sample fired at 1300°C for 5 h and rapidly cooled in air has a smaller lattice parameter (0.4775 $\pm$ 0.0001 nm) than the slightly Co-expelled CaO formed upon slow cooling of the sample in the furnace. The Ca-doped $Co_{1-x}O$ particles were too scarce to give adequate XRD counts for a precise lattice parameter determination.

3.2. AEM

3.2.1. Furnace-cooled samples. Regardless of the firing time, both inter- and intragranular $Co_{1-x}O$ particles were found to contain fine precipitates of Co_3O_4 spinel, i.e., a $2 \times 2 \times 2$ superstructure of $Co_{1-x}O$ as indicated by superlattice spots in the SAED pattern for a representative sample fired at 1300°C for 80 h (Fig. 1).

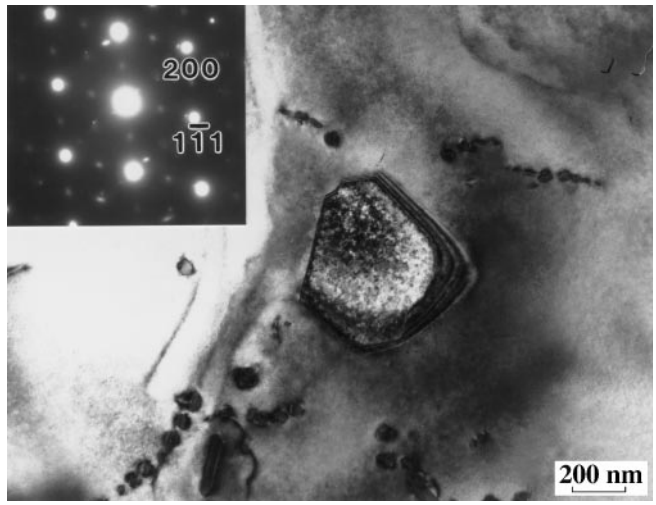

FIG. 1. TEM bright field image (BFI) and inset SAED pattern ([011] zone axis) of intragranular Ca-doped $Co_{1-x}O$ particle with spinel precipitates. The $Co_{1-x}O$/CaO composite was fired at 1300°C for 80 h and cooled in the furnace.

By contrast, the CaO host grains always have paracrystal-type precipitates, not a spinel-type superstructure. These paracrystals were formed at a number of heterogeneous nucleation sites. For example, subgrain boundaries (SGBs) were rather effective sites for nucleating paracrystals (Fig. 2a), which caused side-band diffraction spots to appear next to fundamental spots of rock salt-type structure (Fig. 2b). The spacing of SGB dislocations are too wide (> 100 nm) to account for satellite spots in Fig. 2b. In fact, there is a negligible diffraction intensity beyond first order of the side-band spots, and the spacing of the satellite diffraction spots are approximately 1/8.6 times that of the fundamental spots (e.g., the spot next to 220) of the rock-salt type oxide. Typical misorientation across the SGB was less than 1° according to X and Y tilting angles of the subgrains at two-beam conditions, e.g., in Fig. 2c with the corresponding SAED pattern in Fig. 2d. Dislocations were still the effective nucleation sites of paracrystals for samples fired for a long time (i.e., 80 h) at 1300°C (Fig. 3). The paracrystal precipitates also nucleated and grew at a migrating grain boundary more or less under the influence of a precipitate dragging effect (Fig. 4a), causing cellular structure in the area behind (i.e., swept by) the migrating grain boundary (Fig. 4b). It is noteworthy that the paracrystal precipitates at individual dislocations and grain boundaries give the same satellite spots as those at SGBs, indicating that the satellite spots are indeed due to the structure of the paracrystal precipitates rather than the dislocation networks. This interpretation is

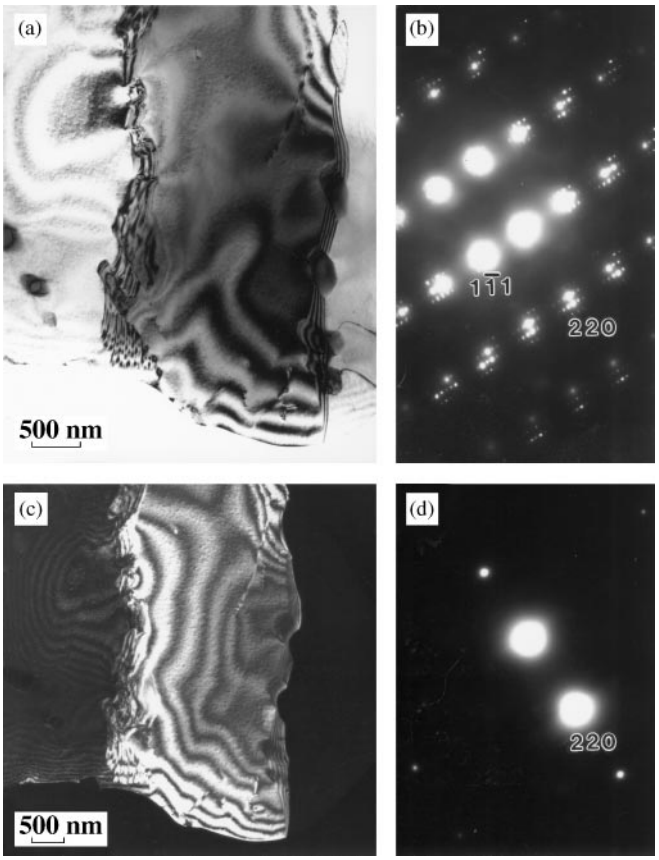

FIG. 2. TEM of a typical Co-doped CaO grain with paracrystalline precipitates at subgrain boundaries: (a) BFI and (b) SAED pattern in the [$\bar{1}$12] zone axis showing fundamental 220 and 1$\bar{1}$1 and satellite spots of rock salt-type structure, (c) dark field image (DFI), and (d) corresponding SAED pattern of a subgrain under two-beam condition with diffracted beam $g = 220$. The $Co_{1-x}O$/CaO composite was fired at 1300°C for 5 h and cooled in the furnace.

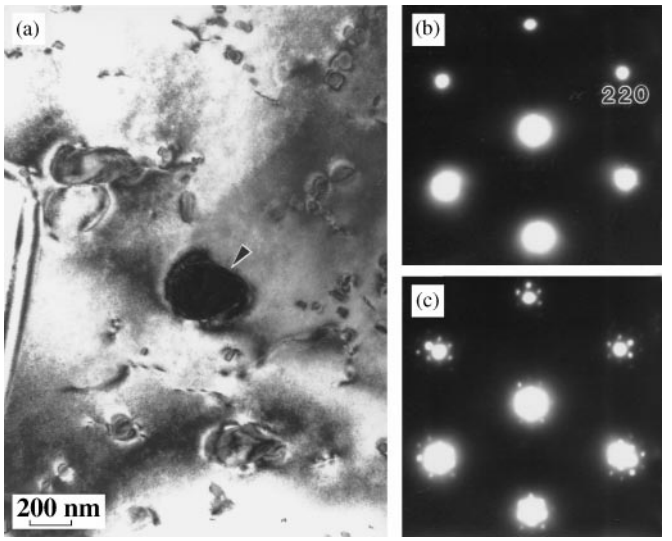

FIG. 3. TEM of Co-doped CaO paracrystals nucleated at dislocations in the $Co_{1-x}O$/CaO composite fired at 1300°C for 80 h and cooled in the furnace: (a) BFI, (b) SAED pattern (in the [$\bar{1}$11] zone axis) from a paracrystal-free area, (c) SAED pattern from a paracrystal (arrow in (a)).

further supported by the observations of air-quenched samples and lattice imaging.

3.2.2. Air-quenched samples. The paracrystal precipitates, with satellite diffraction spots aproximately 1/8.6 times that of the fundamental spots of the rock-salt type oxide, were also identified in the samples air-quenched from 1300°C, indicating the precipitates were formed at 1300°C rather than during cooling. For example, within 5 h at 1300°C such precipitates already nucleated at a migrating grain boundary, causing cellular structure in the area swept by the migrating grain boundary (Fig. 5). The paracrystal precipitates also occurred at SGBs for air-quenched samples (Fig. 6a), as indicated by side-band diffraction spots in the [$\bar{1}$11] zone axis (Fig. 6b) and dark field imaging using such a side-band spot (Fig. 6c).

3.2.3. Lattice image of paracrystals. In Fig. 7 the lattice image of the paracrystalline precipitates at the subgrain boundary, as a representative, shows that the spacing of defect clusters is 8.6 times the *d*-spacing 1$\bar{1}$1 and 220 (2.4 and 2.1 nm, respectively) when viewed in the [$\bar{1}$12] zone axis. Thus, the spacing of defect clusters is nearly 4.3 times the lattice spacing of the average structure of the Co-doped CaO, in accordance with reciprocal space observations. Indeed, the paracrystalline distribution in Fig. 7 is such that the spacing between defect clusters tends to be maintained fairly constant but relative lateral translations occur more variably, as defined by Welberry and Christy (4, 5).

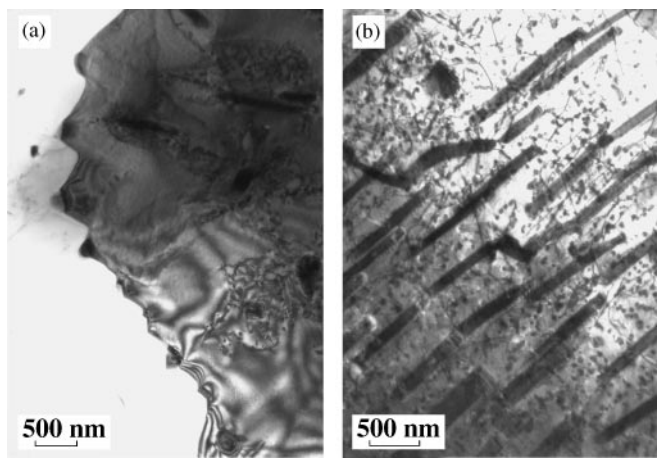

FIG. 4. TEM (BFI) of paracrystalline precipitates nucleated at the grain boundary of Co-doped CaO in the $Co_{1-x}O$/CaO composite fired at 1300°C for 80 h and cooled in the furnace showing: (a) dragging at a migrating grain boundary and (b) cellular structure in the area swept by the migrating grain boundary.

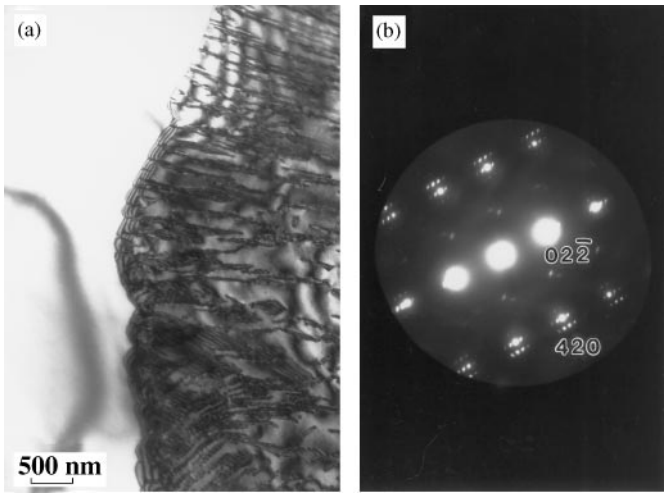

FIG. 5. TEM (a) BFI and (b) SAED pattern in the [$\bar{1}22$] zone axis of cellular precipitates dragging at the grain boundary of Co-doped CaO. The $Co_{1-x}O$/CaO composite was fired at 1300°C for 5 h and air-quenched.

3.2.4. EDX analysis. Point-count EDX analysis indicated that the $Co_{1-x}O$ particles (Fig. 8a) and the CaO matrix (not shown) have about the same (5 mol.%) mutual solid solubility of dopants due to interdiffusion. The paracrystal has a dopant level (approx. 6 mol.%) (Fig. 8b) slightly higher than that of the rest of the area of the CaO host. Since other impurities are negligible in CaO, it should be the Co dopant and resultant defect chemistry that caused the formation of the paracrystal precipitates.

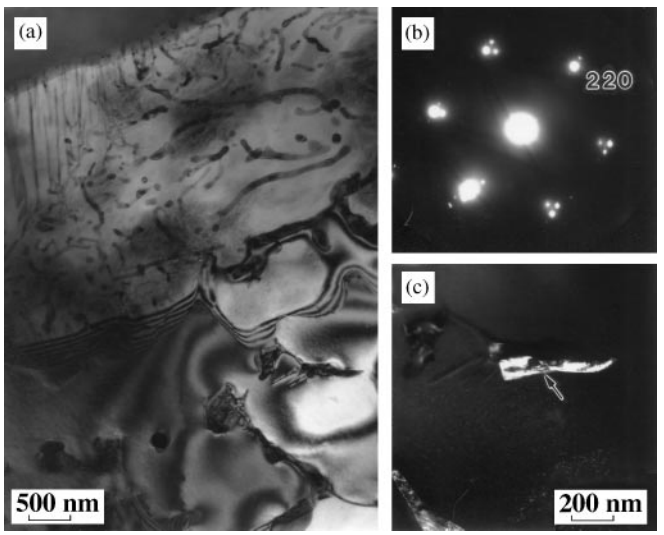

FIG. 6. TEM of paracrystalline precipitates at a subgrain boundary of Co-doped CaO. The $Co_{1-x}O$/CaO composite was fired at 1300°C for 5 h and air-quenched. (a) BFI, (b) SAED pattern ([$\bar{1}11$] zone axis), and (c) DFI of a paracrystal (arrow) taken from (a) and imaged with satellite spot.

FIG. 7. Lattice image of paracrystalline precipitates at a subgrain boundary showing that the spacing of defect clusters is indeed nearly 4.3 times the lattice spacing of the average structure for the Co-doped CaO, i.e., 8.6 times the *d*-spacings 1$\bar{1}$1 and 220 when viewed in the [$\bar{1}12$] zone axis. The $Co_{1-x}O$/CaO composite was fired at 1300°C for 5 h and cooled in the furnace.

4. DISCUSSION

4.1. Defect Chemistry of Cation-Doped $Co_{1-x}O$

4.1.1. Effect of Co^{3+} in $Co_{1-x}O$. Generation of an electron hole in the $Co_{1-x}O$ lattice may proceed through the following equations (27) in Kröger–Vink notation (28):

$$1/2O_2 - V_{Co}^{x} + O_O^{x} \qquad [1]$$

$$V_{Co}^{x} - V'_{Co} + h^{\bullet} \qquad [2]$$

$$V'_{Co} - V''_{Co} + h^{\bullet}. \qquad [3]$$

In this notation, the type of imperfection is indicated by a major symbol, the location is described by a subscript, and finally the charge of the defect relative to the normal lattice

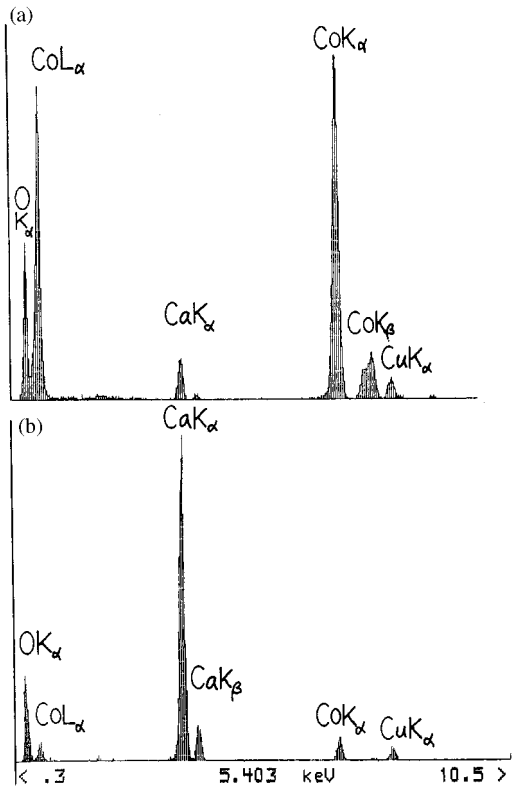

FIG. 8. Point-count EDX spectrum of (a) a Ca-doped $Co_{1-x}O$ particle and (b) the paracrystal precipitate in a Co-doped CaO grain. The $Co_{1-x}O$/CaO composite was fired at 1300°C for 80 h and cooled in the furnace. The Cu peak is due to the supporting Cu ring.

is indicated by a superscript. Here, O_O^x signifies a neutral charged oxygen atom in the normal lattice site; V_{Co}^x, V'_{Co}, and V''_{Co} represents a neutral, single, and double negatively charged cobalt vacancy, respectively; and $h^\bullet$ signifies electron hole (Co_{Co}^{3+} or simplified as $Co_{Co}^{\cdot}$). The singly charged cobalt vacancy V'_{Co} is in fact $[V''_{Co} + Co_{Co}^{\cdot}]$ (V''_{Co} associated with an electron hole localized to form a bound pair of point defects on the octahedral Co sites) analogous to the nature of "singly charged nickel vacancies" in $Ni_{1-x}O$ (29). At temperatures below 900°C, it is expected to increase the Co^{3+}/Co^{2+} ratio through Eqs. [1–3], hence forming a spinel phase Co_3O_4 (19) with cations in both tetrahedral and octahedral sites.

4.1.2. Effect of Ca^{2+} in $Co_{1-x}O$. The present EDX results indicate approx. 5 at.% dissolution of Ca^{2+} in $Co_{1-x}O$. Although the minor $Co_{1-x}O$ particles did not give enough XRD counts for us to estimate a lattice parameter increase as a result of Ca doping, it is conceivable that larger-size Ca^{2+} resides in octahedral substitutional sites rather than interstitial tetrahedral sites of the $Co_{1-x}O$ lattice. The Ca^{2+} (effective ionic radius, 0.1 nm), being larger than Co^{2+} (0.065 nm, low spin) in C.N. 6 (23), is expected to cause volume-compensating defect clusters $[V''_{Co} + Co_{Co}^{\cdot}]$ through the equation

$$CaO \xrightarrow{CoO} Ca_{Co}^x + [V''_{Co} + Co_{Co}^{\cdot}] + h^\bullet + O_O^x. \qquad [4]$$

Here Ca_{Co}^x signifies a noncharged calcium at the cobalt sites in the crystal lattice. It is also possible that the volume-compensating effect due to the substitution of Ca^{2+} with Co^{2+} forced $Co_{Co}^{\cdot}$ to enter the interstitial tetrahedral site, i.e., $Co_i^{\cdot\cdot}$, and hence more charge-compensating cation vacancies through the equation

$$Ca_{Co}^x + [V''_{Co} + Co_{Co}^{\cdot}] \text{—} Ca_{Co}^x + [Co_i^{\cdot\cdot} + 4V''_{Co} + 4Co_{Co}^{\cdot}]. \qquad [5]$$

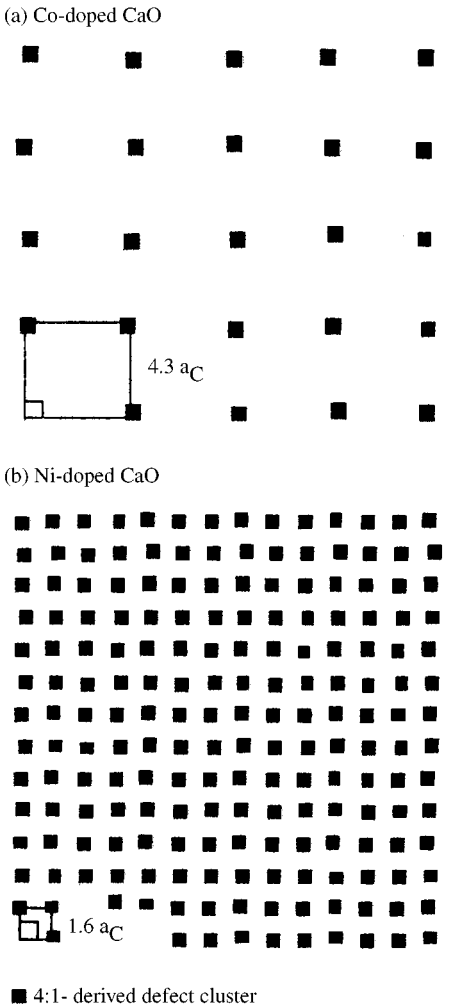

FIG. 9. Schematic drawing ([100] projection in real space) of the paracrystalline distribution of 4:1-type-derived defect clusters (solid squares) with nearly 4.3 and 1.6 times the lattice spacing 0.478 and 0.480 nm (22) of the average structure for (a) Co-doped CaO and (b) Ni-doped CaO (22), respectively.

The 4:1-type defect clusters, a basic structure unit of spinel phase, could be activated through reaction [5]. In this regard, theoretical calculation indicated that an interstitial tetrahedral dopant can stabilize the 4:1 clusters and clusters of 4:1 clusters for 3D transition metal monoxides, e.g., Fe^{3+}-doped $Ni_{1-x}O$ and Mn^{3+}-doped $Co_{1-x}O$ (30). Thus, the Ca^{2+} dopant may stabilize spinel structures at temperatures higher than 900°C, the lower limit for pure $Co_{1-x}O$ as mentioned. The effect of an aliovalent and oversized dopant on stabilizing a spinel structure above 900°C in air has also been observed in Zr^{4+}-doped $Co_{1-x}O$ (20). It should be noted that the paracrystal intermediate was not observed in the Ca-doped $Co_{1-x}O$ particles embedded in the present composites. This may be explained by a rapid phase change of these small-size particles into the spinel structure, with the possible paracrystal intermediate having hardly survived.

4.2. Defect Chemistry of Cation-Doped CaO

4.2.1. Effect of Co^{2+} in CaO. Analogous to the case of the undersized dopant Ni^{2+} in the CaO lattice (22), the Co^{2+} dopant should also substitute for Ca^{2+} in order to have a smaller cell volume, given effective ionic radii of 0.069, 0.065, and 0.100 nm, for Ni^{2+}, Co^{2+} and Ca^{2+}, respectively in C.N. 6 (23). The undersized dopant Co^{2+} in the Ca^{2+} site could also force further Co^{2+} dopants to enter the interstitial site as $Co_i^{\cdot\cdot}$, which then induced charge-compensating cation vacancies and 4:1 defect clusters through the equation

$$CoO \xrightarrow{CaO} Co_{Ca}^{x} + [Co_i^{\cdot\cdot} + 4V_{Ca}'' + 5\,h^{\bullet}] + O_O^x, \quad [6]$$

where $h^{\bullet}$ could be associated with V_{Ca}'' to form V_{Ca}' or associated with Co_{Ca}^{x} (i.e., noncharged cobalt at the calcium site) to form $Co_{Ca}^{\bullet}$. Thus, the 4:1-type defect clusters and the paracrystalline ordered state could be activated through reaction [6]. Oxidation upon cooling below 900°C (19) could somehow facilitate the formation of $Co_i^{\cdot\cdot}$, and hence 4:1-type defect clusters through Eq. [6]. However, this effect may somehow be compensated by the exsolution of thee cobalt dopant upon cooling. According to the phase diagram (24), there is no equilibrium $CaCo_2O_4$-type spinel to be formed at 1300°C or exsolved upon cooling in air, in contrast to the opposite case of Ca-doped $Co_{1-x}O$, which oxidizes spontaneously as the Co_3O_4 spinel when cooled below 900°C in air.

4.2.2. Spacing between defect clusters. The paracrystalline distribution of defect clusters is nearly 4.3 times the lattice spacing of the average structure for the Co-doped CaO (Fig. 9a) as indicated by the spacing of side-band diffraction spots. This spacing between defect clusters is approximately 2.7 times that of our previously studied case of Ni-doped CaO (Fig. 9b) (22). In other words, there is about 20 (i.e., $2.7 \times 2.7 \times 2.7$) times difference in defect-cluster concentration. This may be due to a higher solute content (approx. 10 mol% Ni) and a higher firing temperature (1400°C) of the latter case (22). (The spacing between defect clusters, i.e., the concentration of defect clusters, is indeed affected by dopant level. For example, our previous study indicated the dissolution of approximately 2 mol.% Zr^{4+} caused the paracrystalline distribution of defects nearly 3.5 times the lattice parameter of Zr^{4+}-doped $Ni_{1-x}O$ (17). By contrast, the dissolution of approximately 2 mol.% Zr^{4+} with codopant $Y^{3+} < 0.3$ mol.% led to a paracrystal distribution of defects nearly 2.5 times the lattice parameter (17), i.e., a higher concentration of defect clusters.) Alternatively, the Ni^{2+} dopant is inherently more effective than the Co^{2+} dopant in the CaO lattice for generating defect clusters.

4.3. Nucleation and Growth of Paracrystal during Microstructural Development

Grain boundaries, dislocations, and dislocation arrays at SGBs can be generated by a sintering and coalescence process as demonstrated by the assembly of nanocrystalline titania in solution (31) and the condensation clustering of CeO_2 (32). These lattice imperfections, when developed, might spontaneously act as nucleation sites of the paracrystal precipitates in the present composites. The space charge at these sites, as expected for rock salt-type ionic crystals (33), may favor clustering of the charged species into the 4:1 and paracrystalline ordered state. Alternatively, nucleation of the paracrystal at such sites is beneficial in minimizing strain and/or surface energies and may activate short-circuit diffusion, e.g. a higher diffusivity of cation vacancies at the surface than in the lattice as proved for $Ni_{1-x}O$ (34).

The present experimental results also indicated that the formation of paracrystals was affected by a migrating grain boundary, presumably under the influence of a capillary force and a chemical potential gradient. A beneficial lower nucleation barrier at the grain boundary and a higher growth rate in the grain boundary migrating direction may cause precipitation of cellular paracrystals, analogous to the case of cellular precipitation in metal alloys (35). The essential feature of this type of transformation is that the boundary moves with the growing tips of the precipitates. This kinetic factor accounts for the paracrystal formation in the area just swept by the migrating grain boundary. It should be noted that a composite prepared via a sintering route, as in this case, may show abnormal grain growth. In such circumstances, the so-called isokinetic range of phase change (36) may only be valid in a local area where microstructures of the composites evolved in a more regular manner. Avrami (36) suggested that "a comprehensive description of the phenomena of phase change may be

summarized in phase change, grain number, and microstructure formulas or diagrams, giving, respectively, the transformed volume, grain, and microstructure densities as a function of time, temperature, and other variables." In this regard, a moving grain boundary of Co-doped CaO may more or less cause phantom nuclei at dislocations but may also circumvent site saturation at grain boundaries for paracrystallization to occur.

The paracrystals did not appear to be cellular in the $Ni_{1-x}O$/CaO composite fired at 1400°C (22). It remains to be clarified whether this is simply due to a grain boundary mobility lower than that of the present $Co_{1-x}O$/CaO composite, given a relatively low homologous temperature (i.e., T/T_m in kelvin) as indicated by a higher melting point of $Ni_{1-x}O$ (approx. 2273 K) than of $Co_{1-x}O$ (approx. 2073 K).

5. SUMMARY

1. Analytical electron microscopic observations indicated a paracrystalline array of defect clusters was formed in Co-doped CaO when the $Co_{1-x}O$/CaO powders were sintered and annealed at 1300°C in air.

2. The undersized dopant Co^{2+} resides in the substitutional octahedral and interstitial tetrahedral sites in order to generate volume- and charge-compensating defects for further formation of 4:1-type defect clusters and hence paracrystals in the rock salt-type lattice of CaO.

3. The interspacing of defect clusters is about 4.3 times the lattice spacing of the average rock salt structure of Co-doped CaO. This spacing between defect clusters is about 2.7 times that of our previously studied Ni-doped CaO.

4. The paracrystal predominantly nucleated at dislocations and grain boundaries, and grew along the grain boundary migration direction, causing cellular structure in the area swept by the migrating boundary.

ACKNOWLEDGMENTS

We thank the referees for their comments. This research was supported by the National Science Council, Taiwan, Republic of China.

REFERENCES

1. P. Kofstad, "Nonstoichiometry, Diffusion and Electrical Conductivity in Binary Metal Oxides." Wiley–Interscience, New York, 1972.
2. B. E. F. Fender and F. D. Riley, *in* "The Chemistry of Extended Defects in Non-metallic Solids" (L. Eyring and M. O'Keefe, Eds.), p. 669. North-Holland, Amsterdam, 1970.
3. C. R. A. Catlow and B. E. F. Fender, *J. Phys. C: Solid State Phys.* **8,** 3267 (1975).
4. T. R. Welberry and A. G. Christy, *J. Solid State Chem.* **117,** 398 (1995).
5. T. R. Welberry and A. G. Christy, *Phys. Chem. Miner.* **24,** 24 (1997).
6. P. Vallet and P. Raccah, *Mem. Sci. Rev. Metall.* **62,** 1 (1965).
7. B. Andersson and J. O. Sletnes, *Acta Crystallogr. Sect. A* **33,** 268 (1977).
8. H. G. Sockel and H. Schmalzried, *Ber. Bunsenges. Phys. Chem.* **72,** 745 (1968).
9. C. R. A. Catlow and A. M. Stoneham, *J. Am. Ceram. Soc.* **64,** 234 (1981).
10. R. W. Grime, A. B. Anderson, and A. H. Heuer, *J. Am. Ceram. Soc.* **69,** 619 (1986).
11. W. C. Tripp and N. M. Tallan, *J. Am. Ceram. Soc.* **53,** 531 (1970).
12. M. L. Volpe and J. Reddy, *J. Chem. Phys.* **53,** 1117 (1970).
13. C. M. Osburn and R. W. Vest, *J. Phys. Chem. Solids* **32,** 1331 (1971).
14. R. L. Lalauze and J. H. Meunier, *Oxid. Met.* **12,** 183 (1978).
15. J. Szuber, *J. Mater. Sci.* **19,** 1991 (1984).
16. P. Shen, S. Chen, and H.S. Liu, *Mater. Sci. Eng. A* **161,** 135 (1993).
17. J. Chen and P. Shen, *J. Solid State Chem.* **140,** 361 (1998).
18. S. M. Tomlinson, C. R. A. Catlow and J. H. Harding, *J. Phys. Chem. Solids* **51,** 477 (1990).
19. M. Oku and Y. Sato, *Appl. Surf. Sci.* **55,** 37 (1992).
20. K. T. Lin and P. Shen, *J. Solid State Chem.* **145,** 739 (1999).
21. D. E. Smith, T. Y. Tien, and L. H. van Vlack, *J. Am. Ceram. Soc.* **52,** 460 (1969).
22. M. L. Jeng and P. Shen, *J. Solid State Chem.* **152,** 421 (2000).
23. R. D. Shannon, *Acta Crystallogr. Sect. A* **32,** 751 (1976).
24. A. Muan, *J. Inorg. Nucl. Chem.* **32,** 1457 (1970).
25. B. D. Cullity, "Elements of X-ray Diffraction." Addison-Wesley, Reading, MA, 1978.
26. D. B. Williams, "Practical Analytical Electron Microscopy in Materials Science," p. 157. Philips Electronic Instruments, Electron Optics Publishing Group, Mahwah, NJ, 1984.
27. K. Persels Constant, T. O. Mason, and J. L. Routbort, *J. Phys. Chem. Solids* **53,** 413 (1992).
28. F. A. Kröger and H. J. Vink, *Solid State Phys.* **3,** 307 (1956).
29. A. Atkinson, A. E. Hughes, and A. Hammou, *Philos. Mag. A* **43,** 1071 (1981).
30. R. W. Grime, A. B. Anderson, and A. H. Heuer, *J. Phys. Chem. Solids* **48,** 45 (1987).
31. R. L. Penn and J. F. Banfield, *Science* **281,** 969 (1998).
32. W. H. Lee and P. Shen, *J. Crystal. Growth* **205,** 169 (1999).
33. A. Atkinson and R. I. Taylor, *Philos. Mag. A* **43,** 979 (1981).
34. J. D. Eshelby, C. W. A. Newey, P. L. Pratt, and A. B. Lidiard, *Philos. Mag.* **3,** 75 (1958).
35. D. A. Porter and K. E. Easterling, "Phase Transformations in Metals and Alloys," p. 322. Van Nostrand, London. 1981.
36. M. Avrami, *J. Chem. Phys.* **9,** 177 (1941).